RSC Advances

PAPER

View Article Online
View Journal | View Issue

Check for updates

Cite this: *RSC Adv.*, 2025, **15**, 22930

Received 14th March 2025
Accepted 19th June 2025

DOI: 10.1039/d5ra01820j

rsc.li/rsc-advances

Comparative study of monoclinic and cubic WO_3 nanoplates on NO_2 gas-sensing properties†

Dang Trung Do, *[a] Do Y Nhi Nguyen,[b] Thi Anh Pham,[b] Cong Tu Nguyen *[b] and Van Hieu Nguyen [c]

Monoclinic and cubic WO_3 nanoplates were controllably prepared from orthorhombic $WO_3 \cdot H_2O$ (o-$WO_3 \cdot H_2O$) nanoplates *via* a facile calcination method at 200 °C for 2 hours in ambient air using tubular and muffle furnaces, respectively. The o-$WO_3 \cdot H_2O$ nanoplates were previously prepared from $Na_2WO_4 \cdot 2H_2O$ *via* an acid precipitation method at room temperature. Calcination stimulated the dehydration and phase transformation from hydrated $WO_3 \cdot H_2O$ nanoplates to WO_3 nanoplates, and different crystal structures were observed under different air environments. In an open-air environment (tubular furnace), a stable monoclinic WO_3 (m-WO_3) phase was obtained, while in a closed-air environment (muffle furnace), a high-entropy cubic WO_3 (c-WO_3) phase was obtained. The difference in the phase transformation was confirmed using various physicochemical analyses, such as X-ray diffraction, field emission scanning electron microscopy, Brunauer–Emmett–Teller measurement, diffuse reflectance spectroscopy, and Raman scattering spectroscopy. Both m-WO_3 and c-WO_3 exhibited excellent NO_2 gas-sensing performance, with ultra-high sensitivity, exceptional selectivity, and ultra-low theoretical limit of detection, at a mild optimal-working temperature of 150 °C. In particular, chemiresistive sensors based on m-WO_3 and c-WO_3 nanomaterials exhibited responses of 1322 and 780 to 2.5 ppm NO_2 and theoretical limits of detection of 0.10 and 0.05 ppb to NO_2 at 150 °C, respectively. These results imply that the phase transformation of WO_3 nanostructures or even phase junctions could be achieved *via* a facile calcination process in different controlled environments (in closed or open ambient air) for various designed applications such as gas sensors.

1. Introduction

Recently, air pollution has emerged as a significant global concern, especially in developing countries. Air pollution is mainly attributed to the presence of toxic gases, including NH_3, NO_2, H_2S, CO, and volatile organic chemicals, which are mostly emitted as a result of various human activities.[1,2] Among these gases, NO_2 is one of the most active candidates affecting human health. Hence, advancing the research and development of sensors for detecting low concentrations of these gases is of practical importance for monitoring toxic gas emissions and other related applications.

Various metal oxide semiconductor (MOS) nanomaterials, such as SnO_2, ZnO, TiO_2, In_2O_3 and WO_3, have been developed and extensively studied as gas-sensing materials, demonstrating promising applications in gas sensors.[3–7] Among these MOS nanomaterials, tungsten trioxide (WO_3) is one of the most promising candidates for detecting toxic gases owing to its abundance and excellent chemical stability and electrical conductivity.[8] Tungsten oxide also has high sensitivity to gases including NO_2, H_2, H_2S, NH_3, and CO.[9–13] Notably, WO_3 exhibits outstanding selectivity for NO_2 detection.[14–17] To date, different WO_3 nanostructures, such as nanobelts, nanowires, nanoflakes, nanosheets, and nanofibers, have been fabricated using several methods. Each morphology exhibits good gas-sensing properties for specific target gases.[18–22]

The crystal phase of WO_3 nanomaterials is a key factor influencing the gas-sensing performance of the sensor. Different phases of WO_3 nanostructures, such as monoclinic, orthorhombic, hexagonal (h-WO_3), triclinic, and mixed phases, have been reported recently.[23–28] During the synthesis process, various factors, such as the dosing ratio, reaction temperature, reaction duration, and calcination temperature, can influence the crystalline phase, grain size, and crystal morphology, thereby affecting the gas-sensing performance. Liu and coworkers prepared orthorhombic WO_3 (o-WO_3) nanorods and m-WO_3 *via* a facile hydrothermal synthesis at 180 °C. Results revealed that the m-WO_3-based sensor exhibited a remarkably better response to NO_2 than the o-WO_3-based sensor.[29] Chen

---

[a] *Department of Fundamental of Fire Fighting and Prevention, University of Fire Fighting and Prevention, Hanoi, Vietnam. E-mail: trungdo81@gmail.com*

[b] *Faculty of Engineering Physics, Hanoi University of Science and Technology, Hanoi, Vietnam. E-mail: tu.nguyencong@hust.edu.vn*

[c] *Faculty of Electrical and Electronic Engineering, Phenikaa University, Hanoi, Vietnam*

† Electronic supplementary information (ESI) available. See DOI: **https://doi.org/10.1039/d5ra01820j**

and coworkers prepared and compared the gas sensing performance of o-WO_3 and m-WO_3 nanosheets, which were synthesized by adjusting the synthesis temperature.[30] o-WO_3 nanosheets were formed at temperature below 150 °C, while the transition from orthorhombic to monoclinic occurred at a higher synthesis temperature of 180 °C. The results showed that the m-WO_3 nanosheets exhibited better gas sensitivity than the o-WO_3 nanosheets. L. Zhang and coworkers investigated the gas sensing performance of o-WO_3 and c-/o-WO_3 through a one-step calcination process at temperatures ranging from 500 °C to 1000 °C. The c-/o-WO_3 sample, calcinated at 800 °C, demonstrated a response value of 5.23 to 0.5 ppm of NO_2 and exhibited high selectivity, excellent stability, and reliable repeatability.[31] S. Wei *et al.* fabricated h-WO_3 and o-WO_3 *via* a hydrothermal technique and compared their CO gas-sensing performances. Their findings revealed that variations in the morphology and crystal phase played key roles in the gas-sensing property. The h-WO_3 sensor demonstrated outstanding CO sensing performance at 270 °C and provided a quicker and more enhanced response than that of the o-WO_3 sensor.[27]

Numerous studies have been published on the gas sensing performances of various crystal phases of WO_3 nanostructures. However, up to now, there have been very few reports on comparative studies of the effects of monoclinic and cubic WO_3 nanostructures on NO_2 gas-sensing applications. In this work, monoclinic and cubic WO_3 nanoplates were selectively synthesized from $WO_3 \cdot H_2O$ nanoplates *via* a facile calcination process in regulated environments using different furnaces. Initially, $WO_3 \cdot H_2O$ nanoplates were prepared *via* a facile and power-saving acid precipitation method at room temperature (RT). The effects of the calcination condition on the morphology and crystal structure of samples were investigated using field emission scanning electron microscopy, X-ray diffraction, Brunauer–Emmett–Teller analysis, and diffuse reflectance spectroscopy. The NO_2 gas sensing performance of the sensors were tested using a chemiresistive configuration. Results revealed that both the monoclinic and cubic WO_3 nanoplates exhibited excellent NO_2 gas-sensing characteristics, in which monoclinic WO_3 nanoplates exhibited a better response than those of cubic WO_3 nanoplates. The gas-sensing mechanism and the difference in gas sensing performance of m-WO_3- and c-WO_3-based gas sensors were also discussed.

2. Experimental

2.1. Synthesis of monoclinic and cubic WO_3 nanoplates

Monoclinic and cubic WO_3 nanoplates were prepared from orthorhombic $WO_3 \cdot H_2O$ nanoplates *via* a facile calcination method at 200 °C for 2 hours, in which $WO_3 \cdot H_2O$ nanoplates were previously prepared from $Na_2WO_4 \cdot 2H_2O$ *via* an acid precipitation method. The synthesis procedure is briefly presented in Fig. 1. In detail, a total of 8.25 g of $Na_2WO_4 \cdot 2H_2O$ (Xilong) was first dissolved in 25 mL of distilled water and stirred for 15 minutes to form a clear Na_2WO_4 solution. Subsequently, 20 mL of 65% HNO_3 (Merck) was added, followed by gradual addition of distilled water until the total volume of the precursor suspension reached 80 mL. The suspension was continuously stirred for two hours and then transferred to a Teflon container for acid precipitation at RT. After 24 hours, a yellow slurry was obtained, which was thoroughly rinsed several times with distilled water, and then dried in an oven (Nabertherm oven TR120) at 80 °C for 24 h to produce yellow $WO_3 \cdot H_2O$ aggregates, which were further ground into a powder. The obtained yellow powder was calcined separately in a closed muffle furnace (Nabertherm muffle furnaces L 9/11/B410) and an open tubular furnace (Nabertherm tubular furnace R40/250/12) at 200 °C for 2 hours, yielding white yellow samples, labelled as MF200 and TF200, respectively. The obtained samples were

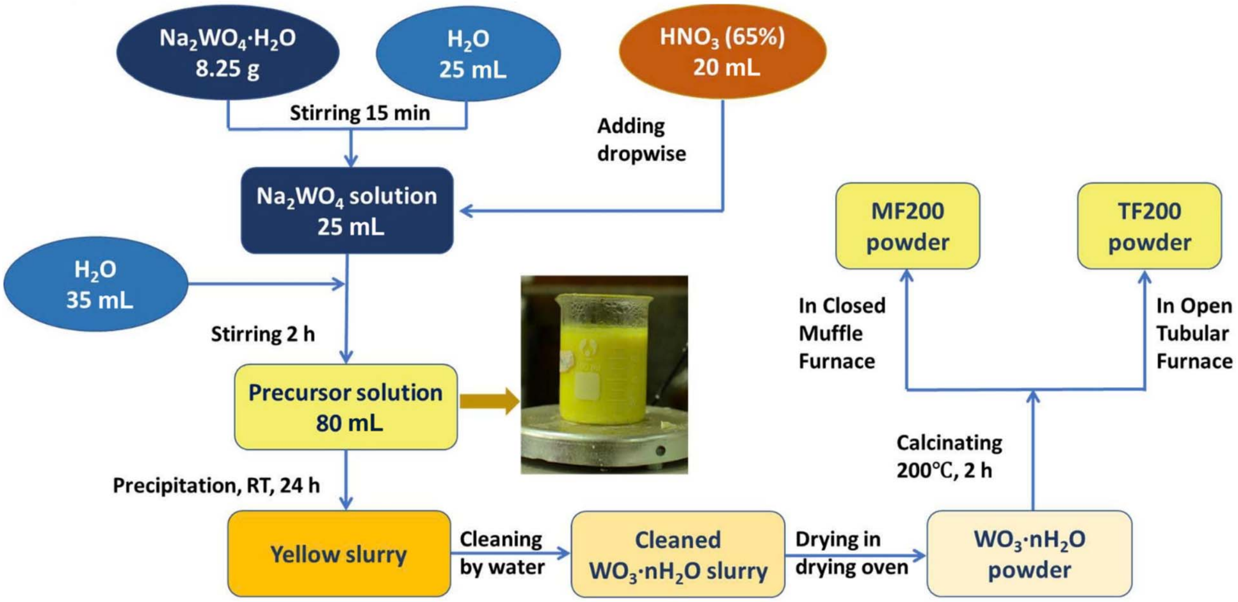

Fig. 1 Schematic of the synthesis process of cubic and monoclinic WO_3 nanostructures.

subsequently utilized for further investigation and evaluation of their gas-sensing performance.

2.2. Physicochemical characterizations

The morphological features of the materials were examined using FESEM (Hitachi S4800). The crystal phases of the WO_3 nanostructures were characterized using X-ray diffraction (XRD) using an X'pert Pro (PANalytical) MPD with Cu-Kα radiation, employing a scanning rate of 0.03° per 2 s. The specific surface areas of the samples were assessed using Brunauer–Emmett–Teller (BET) method, employing a MicroActive for Tristar II Plus 2.03 system. BET measurements were performed using nitrogen adsorption–desorption isotherms at 77 K, and the samples were degassed at 200 °C under vacuum for 6 h prior to the BET analysis. The optical properties of the samples were investigated by analyzing the diffuse reflectance spectra obtained with a JASCO V-750 diffuse reflectance spectrometer (DRS), operating at a scan speed of 400 nm min^{-1}, a bandwidth of 2.0 nm, and a data interval of 0.5 nm.

2.3. Fabrication of gas sensors and their gas-sensing measurements

The chemiresistive gas sensors were prepared from calcinated powders *via* drop-coating method. In detail, 20 mg of white yellow WO_3 powders (TF200 or MF200) was dispersed in 1 mL of dimethylformamide (DMF, Xilong) to obtain a yellow suspension. Subsequently, 0.5 μL of the suspension was drop-coated onto a SiO_2 substrate with interdigitated Pt electrodes on its surface (Fig. S1†). The substrate was then heated at 80 °C in air for 2 minutes. This step was repeated five times. Finally, the sensor was calcined at 200 °C for 2 hours to complete the fabrication process.

The gas-sensing performance of the sensors was assessed through a standard automatic measurement system (Fig. S2†). The resistance of the sensors was measured and recorded with a two-point probe, using a high-precision instrument (Keithley 2602A System SourceMeter) connected to a computer. The concentration of the target gas was controlled by adjusting the volumetric ratio of dried air to the test gas in a standard gas chamber *via* a mass flow controller system. The sensing response (S) was calculated as R_g/R_a for oxidizing gases and R_a/R_g for reducing gases, where R_a and R_g represent the resistance of the sensor when exposed to air and the target gas, respectively.

3. Results and discussion

3.1. Physicochemical properties of the materials

The XRD patterns of the as-synthesized materials are displayed in Fig. 2. The XRD pattern of the as-prepared WO_3 sample is presented in Fig. 2a, which matches well with the standard ICDD card no. 01-084-0886 of o-WO_3, with the (111) plane being dominant. The XRD analysis of the MF200 sample (Fig. 2b) confirmed that all the diffraction peaks closely align with the standard ICDD card no. 00-041-0905 for c-WO_3, exhibiting a lattice constant of 3.84 Å. Specifically, the peaks observed at diffraction angles of 23.9°, 33.98°, 49.25°, 55.25°, and 61.07° correspond to the (100), (110), (111), (200), and (211) crystal planes of c-WO_3, respectively. All the diffraction peaks of the TF200 sample were consistent with the standard pattern for m-WO_3, as given in the standard ICDD card no. 01-089-4476. The peaks at 2θ values of 23.1°, 23.7°, 24.2°, 34.1°, 49°, 56°, and 62°

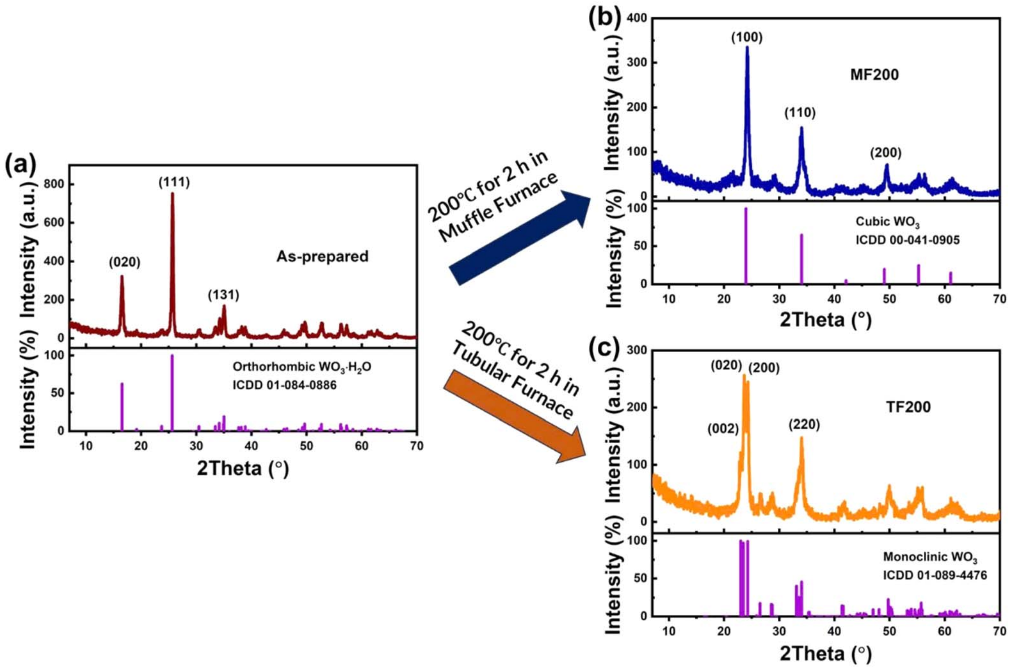

Fig. 2 XRD patterns of the (a) as-prepared WO_3, (b) MF200 and (c) TF200 samples in comparison with standard ICDD cards.

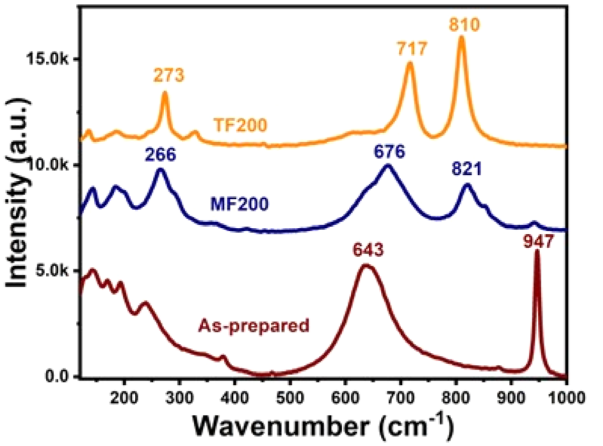

Fig. 3 Raman spectra of the as-prepared WO_3, MF200, and TF200 samples.

correspond to the (002), (020), (200), (220), (113), (133), and (202) crystal facets of m-WO_3, respectively (Fig. 2c). Furthermore, the absence of any additional diffraction peaks indicated that the synthesized samples possessed high phase purity. These results suggested a complete phase transformation from o-$WO_3 \cdot H_2O$ to m-WO_3 and c-WO_3 through simple calcination in an open tubular furnace and a closed muffle furnace at 200 °C for 2 h, respectively. This difference in phase transformations is attributed to variations in the air environment during calcination, which will be discussed in a later section.

Raman spectroscopy is a valuable technique for analyzing the chemical states and crystal structures at the surface of a material. Fig. 3 shows the Raman spectra of the as-prepared and calcined samples, which further confirm the phase transformation from orthorhombic $WO_3 \cdot H_2O$ (as-prepared sample) to cubic WO_3 (MF200) and monoclinic WO_3 (TF200). In detail, the Raman spectrum of the as-prepared material exhibited two

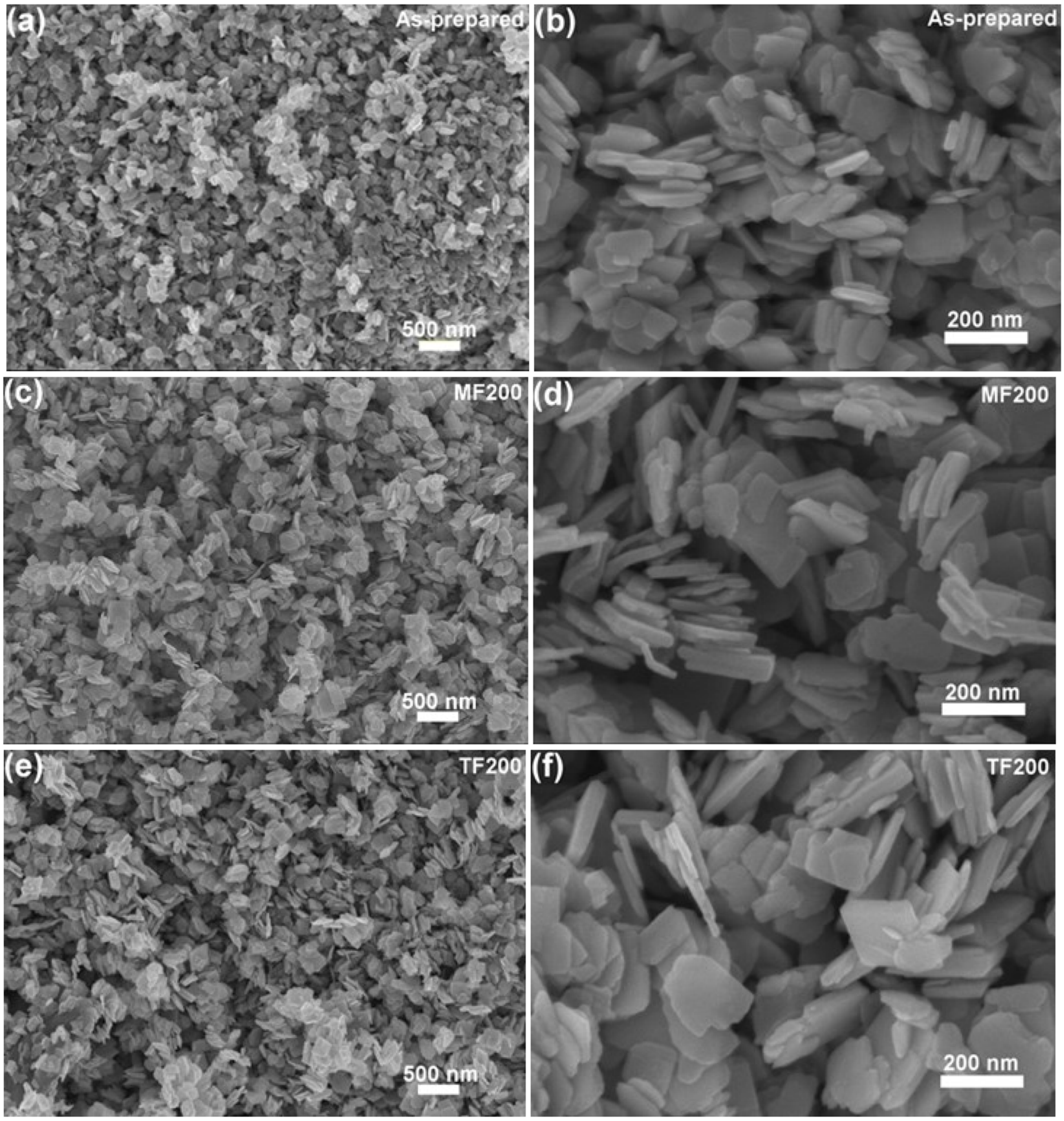

Fig. 4 FESEM images of the as-prepared WO_3 (a and b), MF200 (c and d) and TF200 (e and f) samples observed at different magnifications.

characteristic peaks at 643 cm^{-1} and 947 cm^{-1}, corresponding to the stretching vibrations of the O–W^{6+}–O and W^{6+}=O bonds in orthorhombic $WO_3 \cdot H_2O$, respectively.[32–34] In the Raman spectrum of the sample annealed in a muffle furnace, prominent peaks at 266, 676, and 821 cm^{-1} confirmed the formation of cubic WO_3, and these peaks were assigned to the bending δ(O–W–O) vibration, stretching ν(O–W–O) vibrations in the equator plane and *via* the axis perpendicular to the equator plane of WO_6 octahedra of the O–W–O bonds in cubic WO_3, respectively (note that WO_6 octahedra is the crystal unit in the WO_3 crystal structure).[35,36] Meanwhile, the Raman spectrum of the sample calcined in a tubular furnace showed distinctive peaks at 273, 717, and 810 cm^{-1}, corresponding to the bending δ(O–W–O), stretching ν(O–W–O) modes of O–W–O vibrations in the equator plane and *via* the axis perpendicular to the equator plane of WO_6 octahedra in monoclinic WO_3, respectively, confirming the formation of the monoclinic WO_3 phase.[33,37–39] Notably, in the Raman spectra of c-WO_3, a vibration at ∼940 cm^{-1} was clearly observed, implying the vibration of W^{6+}=O bond in the MF200 (c-WO_3) sample's surface. Besides, the Raman signals were prominent and distinct, which qualitatively confirmed the high crystallinity of both the as-synthesized and calcined samples.

Fig. 4 presents the FESEM images of the samples measured at different magnifications (20 000 and 100 000 times). Results showed that the as-prepared sample has a nanoplate morphology (Fig. 4a and b), which is the preferable morphology of orthorhombic $WO_3 \cdot H_2O$ prepared *via* the acid precipitation method in a highly acidic environment.[32] This nanoplate morphology was well preserved after calcination in both the tubular and muffle furnaces, indicating that the calcination process at 200 °C induced a minimal effect on the morphology of samples. In the calcined samples, the nanoplates appeared to be more separated (less aggregated) than in the as-prepared sample, and the calcinated nanoplates were thinner. In detail, in the MF200 sample, the nanoplates exhibited different dimensions, but most of these nanoplates exhibited an average size of about 250 nm × 200 nm × 40 nm (Fig. 4b and c). In contrast, the TF200 sample contained nanoplates with smooth edges and well-separated structures, with the majority of the larger nanoplates exhibiting an average dimension of ∼200 nm × 200 nm × 30 nm (Fig. 4e and f).

Surface area plays a crucial role in gas-sensing performance, as a larger surface area generally enhances the sensing capability. BET analysis was carried out to evaluate the surface area, pore diameter, and pore volume of the samples (Fig. 5). Results implied that all the samples exhibited the characteristics of type IV isotherms, with similar pore-size distribution patterns (insets of Fig. 5). Specifically, the specific surface areas of the as-prepared c-WO_3 and m-WO_3 nanomaterials were 20.8, 25.0, and 40.6 m^2 g^{-1}, respectively, with corresponding pore volumes of 0.136, 0.146, and 0.178 cm^3 g^{-1} (Fig. 5a–c and Table 1). These

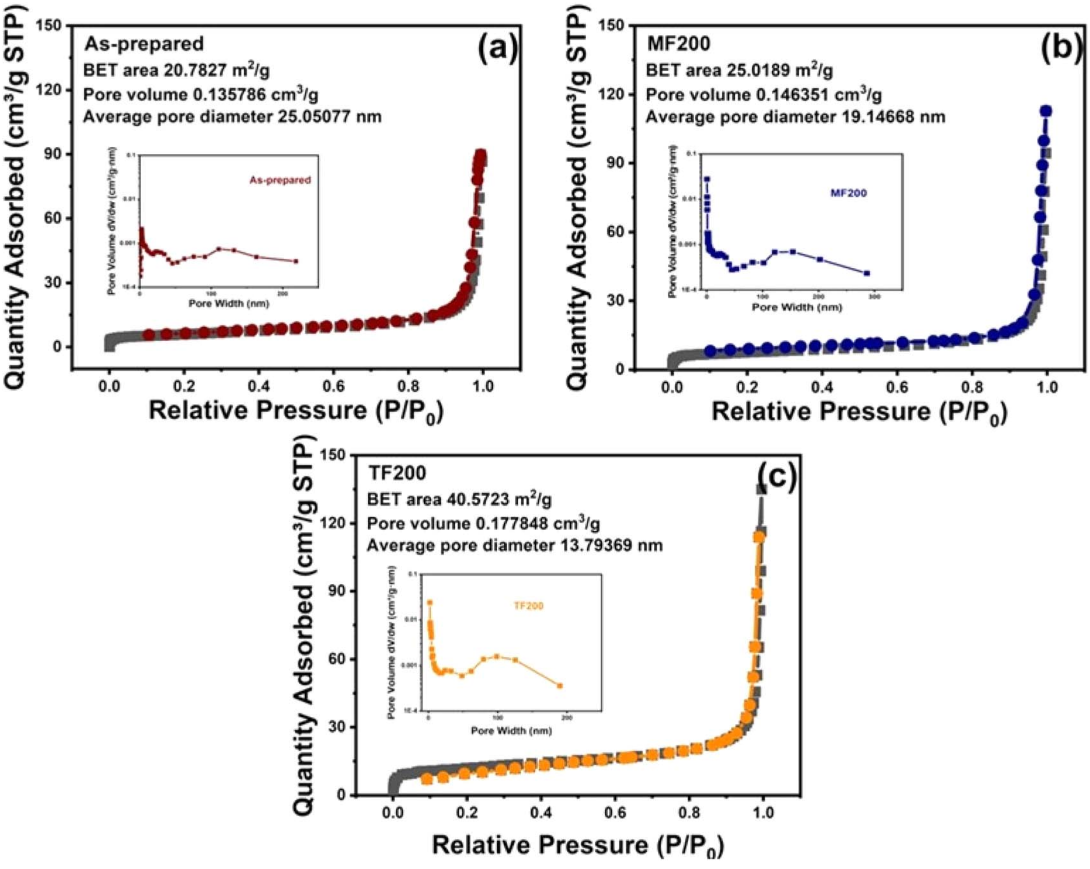

Fig. 5 N_2 adsorption/desorption isotherm and pore size distribution (the inset) of the as-prepared WO_3 (a), MF200 (b) and TF200 (c) samples.

Table 1 BET surface area, pore size, and pore volume of the as-prepared and calcined samples

Samples	BET value ($m^2\ g^{-1}$)	Pore size (nm)	Pore volume ($cm^3\ g^{-1}$)
As-prepared	20.8	25.0	0.136
MF200	25.0	19.1	0.146
TF200	40.6	13.8	0.178

results suggested that calcination increased the surface area. Furthermore, the m-WO_3 nanomaterials exhibited a larger surface area and pore volume than the c-WO_3 nanomaterials, which were beneficial for enhanced gas adsorption and gas-sensing property.

Fig. 6a shows the reflectance spectra of the samples. The as-prepared WO_3 sample effectively reflected visible light in the 550–900 nm range, while MF200 and TF200 exhibited strong reflection over a wider range of 500–900 nm. These results confirmed the phase transformation from o-WO_3 to c-WO_3 and m-WO_3 after calcination. Further analysis using the derived Kubelka–Munk method estimated the optical bandgaps of the as-prepared WO_3, MF200, and TF200 samples to be 2.39 eV, 2.51 eV and 2.69 eV, respectively (Fig. 6b).[38] Furthermore, these results aligned well with the XRD results, where the phase transformation corresponded to the change in optical bandgap.[40]

The formation of orthorhombic $WO_3 \cdot H_2O$ and the phase transformation from o-$WO_3 \cdot H_2O$ to c-WO_3 and m-WO_3 could be explained by the protonation process occurring during the acid precipitation process[32,34] and the dehydration process occurred during the calcination process, respectively.[34,39] In detail, when HNO_3 was introduced into the Na_2WO_4 solution, neutral tungstic acid (H_2WO_4) was first produced, as given in eqn (1):

$$Na_2WO_4 + 2HNO_3 \rightarrow 2NaNO_3 + H_2WO_4 \quad (1)$$

In a highly acidic environment (pH = 1.0, measured by Hanna pH meter model HI2020-02), the high concentration of H^+ promoted the addition of nucleophilic water molecule (H_2O) to tungstic acid, forming a neutral complex $[H_2WO_4(H_2O)_2]^0$ (eqn (2)), which later transformed to a more stable structure of $[WO(OH)_4(OH_2)]^0$ (eqn (3)).[32,34]

$$H_2WO_4 + 2H_2O \xrightarrow{\text{Highly acidic solvent}} [H_2WO_4(H_2O)_2] \quad (2)$$

$$[H_2WO_4(H_2O)_2] \xrightarrow{\text{Highly acidic solvent}} [WO(OH)_4(OH_2)] \quad (3)$$

After neutral seed molecules $[WO(OH)_4(OH_2)]^0$ were formed, the highly acidic environment further promoted the aggregation of seed molecules through van der Waals forces, leading to the development of a $WO_3 \cdot H_2O$ crystalline layer. This layer subsequently transformed into $WO_3 \cdot H_2O$ nanoplates *via* an oxolation process (eqn (4)) during the acid precipitation.

$$[WO(OH)_4(OH_2)] \xrightarrow{\text{Oxolation in highly acidic solvent}} WO_3 \cdot H_2O + 2H_2O \quad (4)$$

Upon calcination at 200 °C, dehydration was stimulated, which resulted in the phase transition from $WO_3 \cdot H_2O$ to cubic WO_3 or monoclinic WO_3 (eqn (5) and (6), respectively).

$$WO_3 \cdot H_2O \xrightarrow{\text{Muffle furnace at 200 °C}} WO_3(\text{cubic}) + H_2O \quad (5)$$

$$WO_3 \cdot H_2O \xrightarrow{\text{Tubular furnace at 200 °C}} WO_3(\text{monoclinic}) + H_2O \quad (6)$$

In the closed furnace (muffle furnace), dehydration was suppressed owing to the closed ambient, which resulted in the formation of high entropy structure of cubic WO_3; the structure is preferably formed at higher temperatures.[41] Alternatively, in an open-air environment, air (especially oxygen) is continuously supplied, endowing the molecules with more freedom to reorganize, resulting in the formation of the stable monoclinic phase.

3.2. Gas-sensing characteristics of the calcined WO_3 nanostructures

The gas-sensing performances were evaluated by monitoring the resistance variation of the sensing material, which

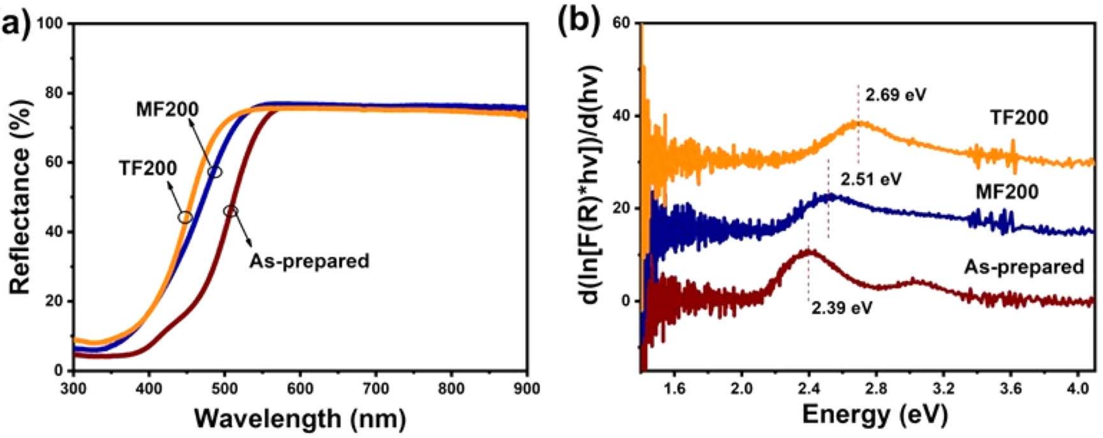

Fig. 6 Comparison of the (a) reflectance spectra and (b) Kubelka–Munk plots of calcined samples with those of the as-prepared sample.

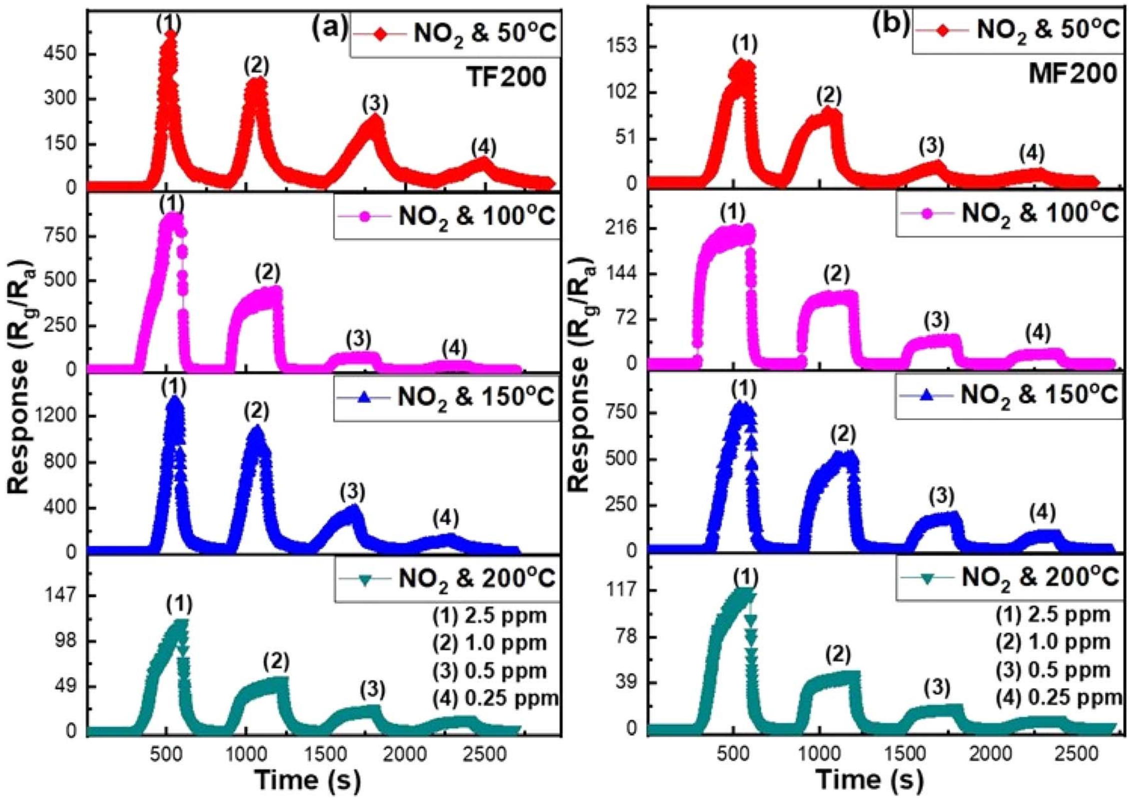

Fig. 7 Gas response changes in the TF200 (a) and MF200 (b) samples towards different concentration of NO_2 gas at 50–200 °C.

depended on the surrounding gas environment and operating temperature, when exposed to the target gases. The response–time curves of the samples were measured in the concentration range of 0.25–2.5 ppm of NO_2 at 50–200 °C, as illustrated in Fig. 7 (the corresponding resistance variation with different NO_2 concentrations at different temperatures are presented in Fig. S3†).

The comparative analysis of the sensing response, response–recovery time, and selectivity between the TF200 and MF200 sensors are indicated in Fig. 8. The effect of temperature on the sensing response was evaluated to identify the optimal working temperature. Fig. 8a presents the sensor response to 2.5 ppm NO_2 across the temperature range of 50–200 °C. Results indicated that the sensing response of the TF200 and MF200 sensors initially increased as the working temperature increased from 50–150 °C and then declined when the working temperature was increased further to 200 °C. This result implied that 150 °C is the optimal working temperature for both the sensors. Fig. 8b exhibits the sensor response to different NO_2 concentrations at 150 °C. The TF200 sensor exhibited average response values of 1322, 1061, 366, and 116 for NO_2 concentrations of 2.5, 1.0, 0.5, and 0.25 ppm, respectively. In contrast, the MF200 sensor showed average response values of 780, 511, 183, and 83 for the same NO_2 concentrations. These results implied that the TF200 sensor possessed a higher gas response capability than that of the MF200 sensor under same conditions. This phenomenon can be attributed to the large specific surface area of the TF200 sensor, which increased the number of active sites compared with the MF200 sample.

The effectiveness and reliability of the sensors were also assessed based on their response/recovery time. The values of the TF200 and MF200 sensors for 2.5 ppm NO_2 at 150 °C are depicted in Fig. 8c. The TF200 sensor exhibited response and recovery times of 239 s and 77 s, whereas the MF200 sensor exhibited response and recovery times of 204 s and 47 s, respectively. Fig. 8d presents the responses of the sensors to 2.5 ppm NO_2 and 100 ppm of different gases, including H_2, ethanol, NH_3 (reducing gas) and H_2S (oxidizing gas) at 150 °C. Results indicated that the response of the sensors to NO_2 is obviously greater than their responses to other gases. This was primarily attributed to the unpaired electrons of NO_2, making it a highly oxidizing and electronegative gas. Accordingly, when it came into contact with WO_3, it readily captured electrons from the surface, leading to a significant increase in the material's resistance. As a result, the sensors demonstrated high selectivity to NO_2 gas.[42] The selectivity of both m-WO_3 and c-WO_3 to NO_2 gas can be attributed to the acidic W surface sites generated *via* the dehydration process, which selectivity adsorbed NO_2.[43,44]

In addition, the repeatability of the m-WO_3 and c-WO_3 sensors for 1 ppm NO_2 at 150 °C is presented in Fig. 9a and b respectively. The dynamic resistance curves exhibited a consistent behaviour across five consecutive test cycles, demonstrating the excellent repeatability of the WO_3 sensors. This further confirmed their potential as reliable candidates for NO_2 detection.

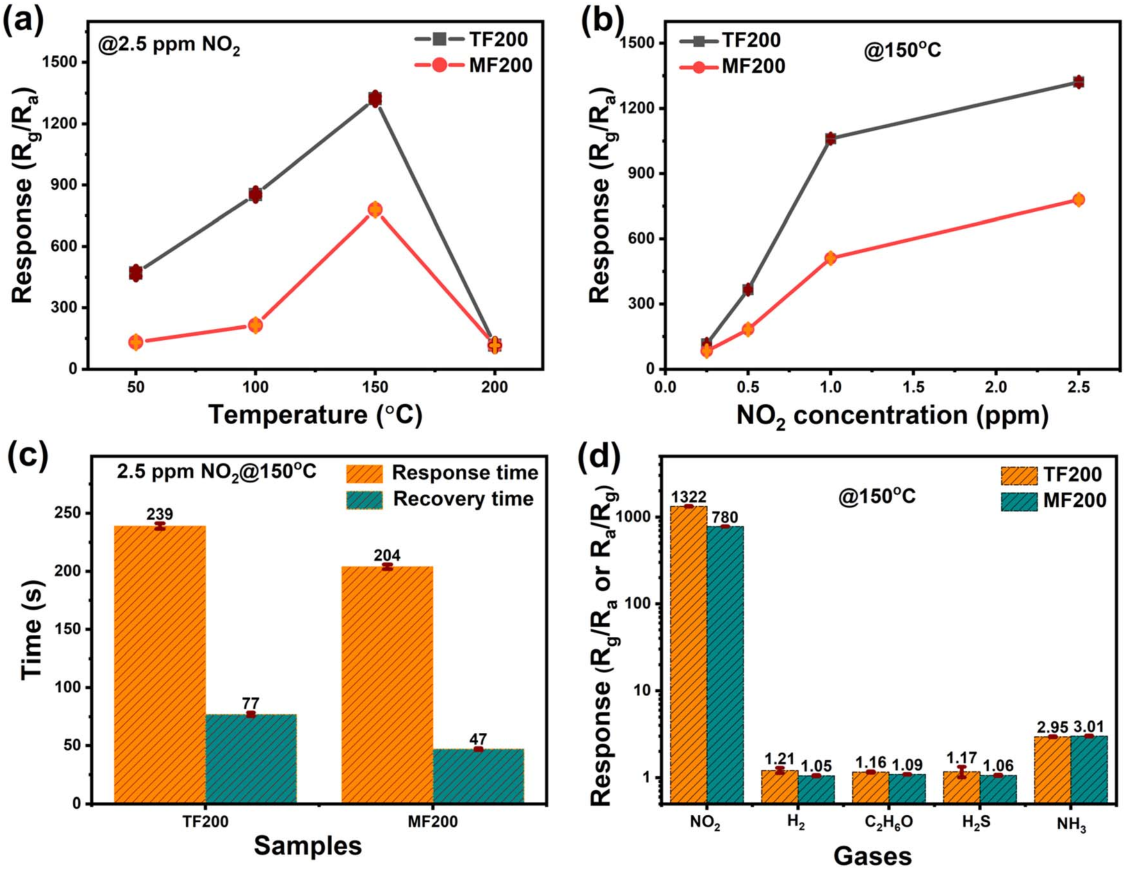

Fig. 8 (a) Response of sensors to 2.5 ppm NO_2 gas at different temperatures; (b) sensitivity of the sensors to different concentrations of NO_2 at 150 °C; (c) response and recovery times of the sensors to 2.5 ppm NO_2 at 150 °C (c); and (d) selectivity of the sensors to 2.5 ppm NO_2, 100 ppm ethanol, 100 ppm H_2, 100 ppm NH_3 and 100 ppm H_2S at 150 °C (reported values are average values with standard deviation).

To evaluate the capability of the sensors, we theoretically estimated its limit of detection using the following equation:[45]

$$\mathrm{LoD} = \frac{3(\mathrm{noise}_{\mathrm{rms}})}{\mathrm{slope}} \tag{7}$$

The slope was derived from the first derivative of the linear section of Fig. 9c; $\mathrm{noise}_{\mathrm{rms}}$ was the root mean square (rms) deviation calculated from a polynomial fit of 50 data points collected when exposed to the air (Fig. S4†). The estimated theoretical detection limits for NO_2 using the m-WO_3 and c-WO_3 sensors were 0.10 ppb and 0.05 ppb, respectively. These results imply that m-WO_3 and c-WO_3 are highly promising materials as NO_2 gas sensors, as they are capable of monitoring NO_2 gas even at sub-ppb level, which is significantly lower than the threshold limit value of 3 ppm established by the American Industrial Hygiene Association.[46]

The NO_2 gas-sensing mechanism of WO_3 nanostructure-based sensors can be described as follows: in an air environment, oxygen molecules absorb on the surface layer of WO_3

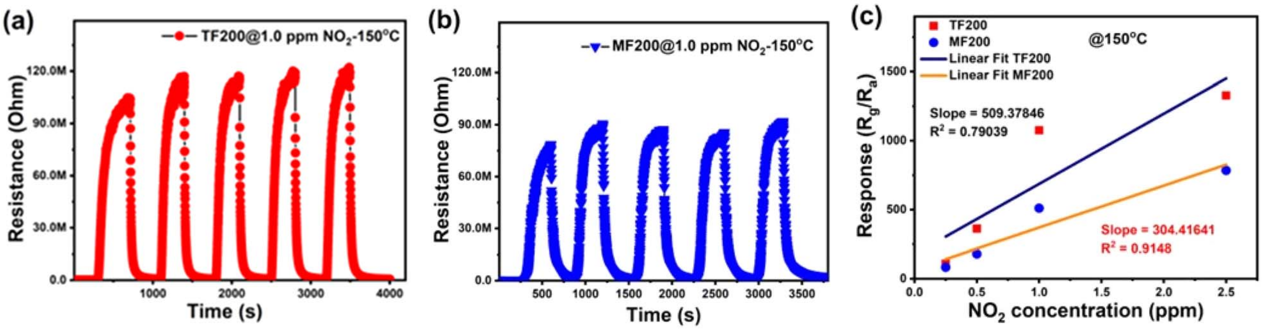

Fig. 9 Repeatability of the TF200 (a) and MF200 (b) sensors to 1 ppm NO_2 at 150 °C and linear fit curve of the gas response *versus* gas concentration at 150 °C for the sensors (c).

Table 2 Comparison of NO_2 gas sensing performance of the sensors based on different phases of the WO_3 nanostructure materials reported in recent literature

Materials	Morphology	Working temp. (°C)	NO_2 conc. (ppm)	Response (R_g/R_a)	τ_{res}/τ_{rec} (s)	Ref.
Triclinic	Nanosheets	200	10	228	7/22	25
			5	150	—	
Hexagonal	Nanorods	75	10	5.8	80/100	50
Orthorhombic	Nanoplates	100	10	17	50/740	51
Monoclinic	Nanoplates	175	5	60	40/130	52
Hexagonal	Nanoflowers	200	100	2.25	12.9/180	53
Monoclinic	Nanoplates	150	2.5	**1322**	239/77	**This work**
Cubic				**780**	204/47	

nanostructure, forming oxygen species (such as O_2^-, O^- and O^{2-}) at different working temperature.[42] These species capture free electrons from the material's conduction band, leading to charge depletion.

$$O_{2(gas)} \rightarrow O_{2(ads)} \tag{8}$$

$$O_{2(ads)} + e^- \rightarrow O_{2(ads)}^- \ (T < 100\ ^\circ C) \tag{9}$$

$$O_{2(ads)}^- + e^- \rightarrow 2O_{(ads)}^- \ (100\ ^\circ C < T < 300\ ^\circ C) \tag{10}$$

$$O_{(ads)}^- + e^- \rightarrow O_{(ads)}^{2-} \ (T > 300\ ^\circ C) \tag{11}$$

During this process, an electron depletion layer develops on the surface of the WO_3 material, leading to a decrease in the charge carrier concentration and an increase in the resistance. As a strong oxidizing agent, NO_2 not only absorbs on the WO_3 nanostructure's surface but also interacts with the oxygen species, as described by the following equation:[47]

$$NO_{2(gas)} + e^- \rightarrow NO_{2(ads)}^- \tag{12}$$

$$NO_{2(ads)}^- + 2O_{(ads)}^- + e^- \rightarrow NO_{2(ads)} + 2O_{(ads)}^{2-} \tag{13}$$

Upon exposure to NO_2 gas, more electrons are extracted from the material, further reducing the charge carrier concentration and widening the electron depletion layer, leading to an increased resistance. Conversely, when NO_2 gas is removed, the electrons previously captured by NO_2 molecules return to the conduction band, shrinking the electron depletion layer and decreasing the resistance.

Notably, c-WO_3 has a narrower optical bandgap and more $W^{6+}{=}O$ bonding on its surface, which theoretically implies better gas-sensing performance than m-WO_3.[9,44,48] However, the experimental results showed the opposite trend. The better gas-sensing performance of m-WO_3 may be attributed to the dominant contribution of its larger surface area and favorable nanoplate morphology;[46,49] m-WO_3 (TF200) possessed nearly twice the surface area of c-WO_3 (MF200).

Table 2 compares the NO_2 gas-sensing performance of WO_3-based sensors in different phases.[25,50–53] Among the reported NO_2 gas sensors, those based on m-WO_3 and c-WO_3 exhibited excellent sensitivity at 150 °C, demonstrating high response levels and indicating their potential as candidates for NO_2 gas detection.

4. Conclusions

Monoclinic and cubic WO_3 nanoplates were controllably prepared from orthorhombic $WO_3 \cdot H_2O$ nanoplates *via* a facile calcination process at 200 °C for 2 hours in a tubular furnace and a muffle furnace, respectively. XRD, BET, Raman, and DRS results showed that the calcination process stimulated dehydration in both the furnaces, which resulted in the phase transformation of hydrated $WO_3 \cdot H_2O$ nanoplates into WO_3 nanoplates. However, different atmospheric environments led to distinct crystal structures. Specifically, under open-air condition (tubular furnace), o-$WO_3 \cdot H_2O$ was transformed into a stable monoclinic crystal structure, m-WO_3 (TF200), with a surface area of 40.6 $m^2\ g^{-1}$. In contrast, under closed-air environment (muffle furnace), o-$WO_3 \cdot H_2O$ was converted into a high-entropy cubic crystal structure, c-WO_3 (MF200), with a surface area of 25.0 $m^2\ g^{-1}$. Notably, both m-WO_3 and c-WO_3 demonstrated excellent gas-sensing characteristics, with ultra-high response, exceptional selectivity, and ultra-low theoretical detection limits, at a mild optimal working temperature of 150 °C. At this temperature, the m-WO_3 and c-WO_3 sensors exhibited average responses of 1322 and 780 to 2.5 ppm NO_2 with theoretical detection limits of 0.10 and 0.05 ppb, respectively. The better NO_2 gas-sensing characteristic of m-WO_3 than that of c-WO_3 was mainly attributed to its larger surface area. This work presents a useful method for the controlled synthesis of WO_3 nanostructures with distinct crystal structures, offering promising potential for various sensing applications.

Data availability

The data used to support the findings of this study are available from the corresponding author upon reasonable request.

Author contributions

Dang Trung Do: investigation, methodology, visualization, formal analysis, writing – original draft. Do Y Nhi Nguyen: investigation, formal analysis. Thi Anh Pham: investigation, formal analysis. Cong Tu Nguyen: conceptualization, methodology, formal analysis, writing – review and editing, validation. Van Hieu Nguyen: supervision, validation.

Conflicts of interest

The authors declare no conflict of interest.

Acknowledgements

The authors (Do Y Nhi Nguyen and Cong Tu Nguyen) would like to thank the financial support from the Asahi Glass Foundation and Hanoi University of Science and Technology (HUST) through the project number AGF.2024-04.

References

1 S. W. Lee, H. G. Jung, J. W. Jang, D. Park, D. Lee, I. Kim, Y. Kim, D. Y. Cheong, K. S. Hwang, G. Lee and D. S. Yoon, *Sens. Actuators, B*, 2021, **345**, 130361.

2 Y. Li, M. Dai, J. Bai, Y. Wang, Y. Li, C. Wang, F. Liu, P. Sun, T. Wang and G. Lu, *Sens. Actuators, B*, 2022, **370**, 132398.

3 Y. Ding, B. Du, X. Guo, Y. Dong, M. Zhang, W. Jin, C. Gao, D. Peng and Y. He, *Sens. Actuators, B*, 2024, **414**, 135916.

4 M. Jiao, N. Van Duy, D. D. Trung, N. D. Hoa, N. Van Hieu, K. Hjort and H. Nguyen, *J. Electron. Mater.*, 2018, **47**, 785–793.

5 K. Iwata, H. Abe, T. Ma, D. Tadaki, A. Hirano-Iwata, Y. Kimura, S. Suda and M. Niwano, *Sens. Actuators, B*, 2022, **361**, 131732.

6 S. B. Patil, M. A. More, D. Y. Patil, F. I. Ezema and G. E. Patil, *Mater. Lett.*, 2025, **382**, 137882.

7 Q. Wang, R. Li, P. Wang, Y. Zhang, Y. Wang, Y. Yang, Z. Wu, B. An, J. Li and E. Xie, *Sens. Actuators, B*, 2023, **390**, 133985.

8 Z. F. Huang, J. Song, L. Pan, X. Zhang, L. Wang and J. J. Zou, *Adv. Mater.*, 2015, **27**, 5309–5327.

9 K. K. Devender, B. Palanisamy, A. Jayaram, N. Mani and H. Santhana Krishnan, *ACS Appl. Nano Mater.*, 2024, **8**(1), 65–79.

10 R. B. T, P. V. K. Yadav, A. Mondal, K. Ramakrishnan, J. Jarugala, C. Liu and Y. A. K. Reddy, *Chemosphere*, 2024, **353**, 141545.

11 Y. Qin, Y. Zhang, J. Lei and S. Lei, *Sens. Actuators, B*, 2025, **428**, 137239.

12 L. Jian, R. Peng, Y. He, X. Wang and W. Guo, *Mater. Lett.*, 2023, **336**, 133897.

13 L. Piliai, T. N. Dinhová, M. Janata, D. Balakin, S. Vallejos, J. Otta, J. Štefková, L. Fišer, P. Fitl, M. Novotný, J. Hubálek, M. Vorochta, I. Matolinová and M. Vrňata, *Sens. Actuators, B*, 2023, **397**, 134682.

14 M. Wang, Y. Wang, X. Li, C. Ge, S. Hussain, G. Liu and G. Qiao, *Sens. Actuators, B*, 2020, **316**, 128050.

15 F. Liu, H. Song, L. Wu, J. Zhao, X. Yao, K. Fu, Z. Jin, J. Liu, F. Wang and Z. Wang, *Colloids Surf., A*, 2023, **666**, 131329.

16 D. Kanchan Kumar, P. Bharathi, J. Archana, M. Navaneethan and S. Harish, *Sens. Actuators, B*, 2024, **421**, 136477.

17 Z. Wan, C. Ge, L. Bai, S. Hussain, G. Liu, G. Qiao and M. Wang, *Ceram. Int.*, 2024, **50**, 36900–36907.

18 H. L. Yu, J. Wang, B. Zheng, B. W. Zhang, L. Q. Liu, Y. W. Zhou, C. Zhang and X. L. Xue, *Sens. Actuators, A*, 2020, **303**, 111865.

19 S. Bonam, V. R. Naganaboina, B. Thirupathi and S. G. Singh, *J. Mater. Sci.: Mater. Electron.*, 2024, **35**, 1–12.

20 X. Wang, X. Meng and W. Gao, *Sens. Actuators, B*, 2023, **387**, 133790.

21 B. An, Y. Yang, J. Yan, Y. Wang, R. Li, Z. Wu, T. Zhang, R. Han, X. Cheng, Q. Wang and E. Xie, *Appl. Surf. Sci.*, 2025, **692**, 162722.

22 S. Cao, C. Zhao, T. Han and L. Peng, *Mater. Lett.*, 2016, **169**, 17–20.

23 S. Tripathi, D. Tripathi, R. K. Rawat and P. Chauhan, *Mater. Lett.*, 2023, **335**, 133840.

24 W. Zeng, B. Miao, T. Li, H. Zhang, S. Hussain, Y. Li and W. Yu, *Thin Solid Films*, 2015, **584**, 294–299.

25 L. Han, J. Chen, Y. Zhang, Y. Liu, L. Zhang and S. Cao, *Mater. Lett.*, 2018, **210**, 8–11.

26 H. H. Afify, S. A. Hassan, M. Obaida, I. Moussa and A. Abouelsayed, *Opt. Laser Technol.*, 2019, **111**, 604–611.

27 S. Wei, J. Zhao, B. Hu, K. Wu, W. Du and M. Zhou, *Ceram. Int.*, 2017, **43**, 2579–2585.

28 F. Liu, H. Song, L. Wu, J. Zhao, X. Yao, K. Fu, Z. Jin, J. Liu, F. Wang and Z. Wang, *Colloids Surf., A*, 2023, **666**, 131329.

29 Z. Liu, M. Miyauchi, T. Yamazaki and Y. Shen, *Sens. Actuators, B*, 2009, **140**, 514–519.

30 Y. Chen, K. Xue and Z. Wang, *Mater. Sci. Semicond. Process.*, 2025, **188**, 109211.

31 L. Zhang, F. Li, Y. Yang, D. Li, H. Yu, X. Dong and T. Wang, *Microchem. J.*, 2024, **205**, 111243.

32 N. L. Pham, T. L. A. Luu, H. L. Nguyen and C. T. Nguyen, *Mater. Chem. Phys.*, 2021, **272**, 125014.

33 M. F. Daniel, B. Desbat, J. C. Lassegues, B. Gerand and M. Figlarz, *J. Solid State Chem.*, 1987, **67**, 235–247.

34 N. L. Pham, T. L. A. Luu, T. T. M. Nguyen, V. T. Pham, H. L. Nguyen and C. T. Nguyen, *Commun. Phys.*, 2022, **32**, 307–318.

35 G. N. Kustova, Y. A. Chesalov, L. M. Plyasova, I. Y. Lin and A. I. Nizovskii, *Vib. Spectrosc.*, 2011, **55**, 235–240.

36 J. De Ribamar Martins Neto, R. M. Torresi and S. I. Cordoba De Torresi, *J. Electroanal. Chem.*, 2016, **765**, 111–117.

37 X. V. Le, T. L. A. Luu, H. L. Nguyen and C. T. Nguyen, *Vacuum*, 2019, **168**, 108861.

38 C. T. Nguyen, T. P. Pham, T. L. A. Luu, X. S. Nguyen, T. T. Nguyen, H. L. Nguyen and D. C. Nguyen, *Ceram. Int.*, 2020, **46**, 8711–8718.

39 V. T. Nguyen, H. S. Nguyen, V. T. Pham, T. T. M. Nguyen, T. L. A. Luu, H. L. Nguyen, D. C. Nguyen and C. T. Nguyen, *Commun. Phys.*, 2020, **30**, 319–330.

40 M. J. Priya, P. P. Subha, A. Antony, M. K. Jayaraj and K. Rajeev Kumar, *Chem. Phys. Lett.*, 2023, **829**, 140749.

41 N. A. Mohd Razali, W. N. Wan Salleh, F. Aziz, L. W. Jye, N. Yusof and A. F. Ismail, *J. Cleaner Prod.*, 2021, **309**, 127438.

42 K. Gu, X. Song, Q. Zhang and M. Zhang, *Sens. Actuators, B*, 2023, **382**, 133453.

43 M. Epifani, *Sensors*, 2022, **22**, 2247.

44 R. Li, Q. Wang, Y. Wang, B. An, Y. Yang, Z. Wu, P. Wang, T. Zhang, R. Han and E. Xie, *ACS Appl. Mater. Interfaces*, 2024, **16**, 51738–51747.

45 M. J. Priya, C. S. Saramgi, P. P. Subha, A. Antony, M. K. Jayaraj and K. Rajeev Kumar, *Surf. Interfaces*, 2024, **48**, 104340.

46 Y. Li, Q. Zhou, S. Ding and Z. Wu, *Front. Chem.*, 2021, **9**, 1–8.

47 S. S. Sangale, V. V. Jadhav, S. F. Shaikh, P. V. Shinde, B. G. Ghule, S. D. Raut, M. S. Tamboli, A. M. Al-Enizi and R. S. Mane, *Mater. Chem. Phys.*, 2020, **246**, 122799.

48 G.-L. Chen, H.-Y. Jiang, Z.-P. Deng, Y.-M. Xu, L.-H. Huo and S. Gao, *Sens. Actuators, B*, 2024, **415**, 135981.

49 M. Epifani, *Sensors*, 2022, **22**(6), 2247.

50 Y. Shen, H. Bi, T. Li, X. Zhong, X. Chen and A. Fan, *Appl. Surf. Sci.*, 2018, **434**, 922–931.

51 S. S. Shendage, V. L. Patil, S. A. Vanalakar, S. P. Patil, N. S. Harale, J. L. Bhosale, J. H. Kim and P. S. Patil, *Sens. Actuators, B*, 2017, **240**, 426–433.

52 T. Li, Y. Shen, X. Zhong, S. Zhao, G. Li, B. Cui, D. Wei and K. Wei, *J. Alloys Compd.*, 2020, **818**, 152927.

53 G. M. Hingangavkar, Y. H. Navale, T. M. Nimbalkar, R. N. Mulik and V. B. Patil, *Sens. Actuators, B*, 2022, **371**, 132584.